INSTITUT DE FRANCE
Académie des sciences

Comptes Rendus

Mécanique

Daniel Resende Gonçalves, José dos Reis Vieira de Moura Jr., Paulo Elias Carneiro Pereira, Marcos Vinícius Agapito Mendes and Henrique Senna Diniz-Pinto

Indicator kriging for damage position prediction by the use of electromechanical impedance-based structural health monitoring

Volume 349, issue 2 (2021), p. 225-240

Published online: 27 April 2021

https://doi.org/10.5802/crmeca.81

Les Comptes Rendus. Mécanique *sont membres du Centre Mersenne pour l'édition scientifique ouverte*
www.centre-mersenne.org
e-ISSN : 1873-7234

Comptes Rendus
Mécanique
2021, 349, nº 2, p. 225-240
https://doi.org/10.5802/crmeca.81

Short paper / *Note*

Indicator kriging for damage position prediction by the use of electromechanical impedance-based structural health monitoring

Daniel Resende Gonçalves [a], José dos Reis Vieira de Moura Jr. [a], Paulo Elias Carneiro Pereira [*, b], Marcos Vinícius Agapito Mendes [b] and Henrique Senna Diniz-Pinto [b]

[a] Mathematics and Technology Institute, Federal University of Catalão, 1120 Dr. Lamartine Pinto de Avelar Av., Catalão, 75704-020, Brazil

[b] Engineering School, Federal University of Catalão, 1120 Dr. Lamartine Pinto de Avelar Av., Catalão, 75704-020, Brazil

E-mails: danielresendeg@gmail.com (D. R. Gonçalves), zereis@ufg.br (J. R. V. Moura Jr.), paulo_elias_carneiro@ufg.br (P. E. C. Pereira), marcos.vinicius@ufg.br (M. V. A. Mendes), henriquesenna@ufg.br (H. S. Diniz-Pinto)

Abstract. Some nondestructive techniques of the Structural Health Monitoring (SHM) have improved their analysis in the past decades. Among them, the electromechanical impedance-based SHM technique (EMI-SHM) has been tested in several fields and associated to different statistical methodologies. Considering the nature of the spatial variation of the damage metric data along structures, herein is proposed the use of the indicator kriging method for predicting the existence of a known damage located in the center of an aluminum plate. Maps showing the probability of the damage metric to fall in several value ranges were capable of outlining the areas affected by the damage and predict its location. Comparisons between scenarios with different spacing between PZT patches showed a reduction in the reliability of the model with the increasing of such spacing. Also, for the structure under study, it demonstrates that it is not possible to obtain results by the methodology for distance between sensors/actuators greater than 16.67 cm. However, the results show that this approach can be a viable alternative for using damage metrics to map regions affected by damage and its location.

Keywords. Control of mechanical systems, Indicator kriging, Impedance-based SHM, Damage detection technique, Semivariogram.

2020 Mathematics Subject Classification. 70Q99.

Manuscript received 25th July 2020, revised and accepted 26th March 2021.

* Corresponding author.

1. Introduction

Structures and/or machineries operate under severe mechanical conditions (static and/or dynamic loadings), and are subjected to environmental ones, such as temperature, humidity, and/or chemical [1]. A combination of these factors leads to occurrence of structural failures, caused by damages, needing to be monitored and analyzed with the aim of predicting them (diagnosis and prognosis), which is the goal of the Structural Health Monitoring (SHM) techniques and tools.

Electromechanical impedance-based SHM technique (EMI-SHM) is of special interest due to its low cost in relation to the other ones, and its nondestructive character. This approach has been applied in several situations and purposes, such as pipelines [2, 3], aircraft structures [4–8], hardened cement pastes or concrete structures [9–15], composite materials [16, 17], and steel-made objects or structures [18].

Among other issues, damage detection in EMI technique involves its localization and its severity quantification, which is crucial information for the decision-making process. Several approaches are in development for the damage's localization.

Some approaches include decoupling measurements of piezoelectric transducers [19], which is based on extracts of only the electrical contributions of the structure, applying an artificial neural network [5, 8, 20]; using a direct-coupled mechanical impedance extraction methodology associated with a probability-weighted function [21], triangulation based on the mapping of the correlation between impedance signatures and its distance from the damage [22], interpolation of damage metrics using inverse distance weighting [23], and interpolation based on ordinary kriging method [24].

Results derived from the aforementioned articles, particularly those of Kravolec *et al.* [22], Cherrier *et al.* [23], and Gonçalves *et al.* [24] show the existence of a correlation between the impedance signatures issued by PZT patches and their distance from the damage. It is shown that damage metric values vary gradually along a surface, from high damage metric values near the damage, to low ones, far from the damage location. Considering this nature of the impedance signatures, in this study, the indicator kriging method is applied for mapping the position of a known damage in a square plate of 100 cm based on numerical data similar to real ones. This goal can be achieved by evaluating the probabilities of the damage data to be higher than specific values (thresholds), particularly, the extreme ones. In order to evaluate the influence of the spacing between PZT patches in the indicator kriging method, five spacing scenarios in regular meshes are tested: (1) 9.09 cm × 9.09 cm; (2) 11.11 cm × 11.11 cm; (3) 14.286 cm × 14.286 cm; (4) 16.67 cm × 16.67 cm; and (5) 20.0 cm × 20.0 cm.

2. Theoretical background

2.1. *SHM based on electromechanical impedance*

The EMI method used for SHM is based on the interaction between the electrical impedances of the structure being monitored and piezoelectric sensors, commonly those constituted of lead zirconate titanate (PZT), coupled to it [25, 26].

Electromechanical models were formulated with the aim of describing the relationship between the structure and the piezoelectric transducer. Liang *et al.* [27] define the transducer's electric impedance $Z_E(\omega)$ associated with the structure's mechanical impedance $Z_s(\omega)$ by (1). In this model, $Z_p(\omega)$ corresponds to the transducer's mechanical impedance; ω is the angular frequency; τ, a geometric constant; ϵ_{33}^T, dielectric constant for a constant mechanical stress (T); Y_{XX}^E,

Young's modulus for a constant electric field (E); d_{3X}^2, a dielectric constant; and j, an imaginary unit.

$$Z_E(\omega) = \frac{1}{\mathrm{j}\omega\tau}\left(\epsilon_{33}^T - \frac{Z_s(\omega)}{Z_s(\omega)+Z_p(\omega)} d_{3X}^2 Y_{XX}^E\right)^{-1}. \tag{1}$$

Changes in the structure's mechanical impedance due to a failure lead to a modification of the signal (electric impedance) issued by PZT patches coupled to the structure, whose signal is measured within a frequency range. Changes in the structural conditions are identified through comparison between impedance signatures before and after a failure occurrence [4, 28–32].

Quantitative analysis of the damage is obtained through damage index. Among them, the Root Mean Square Deviation (RMSD), expressed by (2), is the most common, which measures the similarity/correlation between values located at the same frequency point, and grounded in the Euclidean norm [33, 34]. The occurrence of the structural failure is based on comparing the electrical impedance before ($Z_E^0(k)$) and after ($Z_E(k)$), all of them measured in several k points in the frequency domain, whose range varies from ω_I (initial frequency) to ω_F (final frequency).

$$\mathrm{RMSD} = \sqrt{\frac{\sum_{k=\omega_I}^{\omega_F}[Z_E(k) - Z_E^0(k)]^2}{\sum_{k=\omega_I}^{\omega_F}[Z_E^0(k)]^2}}. \tag{2}$$

Damage metrics measured along several locations on the structure enables the mapping of its influence, providing information for the decision-making process relating to maintenance programs.

2.2. *Geostatistics and indicator kriging*

In the articles of Georges Matheron [35–37], geostatistics had its formulation as an application of the Theory of Regionalized Variables, with the initial aim of solving problems related to spatially correlated data in areas of Geology and Mining Engineering, in which sample data need to be spatially interpolated, resulting in models used for a decision-making process.

The variables handled by geostatistical techniques are characterized by having a spatial (or spatio-temporal) continuity along the domain being analyzed [38], in such a way that spatial data close to each other have similar values, which become more different with the increase in the distance separating the spatial data. This implies that not only the value of the variable is considered in the analysis, but also its relative position in the space [39], leading to the quantification of the spatial correlation of the sampled values, done by the semivariogram function (3).

$$\gamma(h) = \frac{1}{2N(h)} \sum_{i=1}^{N(h)} [z(x_i) - z(x_i+h)]^2. \tag{3}$$

The semivariogram ($\gamma(h)$) quantifies the half of the mean squared differences between two spatial data ($z(x_i)$ and $z(x_i+h)$) separated from each other by a distance (vector) h [40]. Computation of the semivariogram for several classes of distances in a specific spatial direction provides an inventory of the continuity in this one in the form of a plot (experimental semivariogram) comparing the semivariance values ($\gamma(h)$) and their respective distance class (Figure 1). Its characteristic of being a growing function reflects the progressive loss of spatial continuity in such direction [38, 41, 42].

Experimental semivariograms need to be fitted by mathematical functions for their use in the estimation process (kriging equations). The reasons for this involve several aspects, whose discussions can be found in [39, 40, 43]. A semivariogram model can consist of one or more simple mathematical functions, depending on the shape of the experimental semivariogram [44].

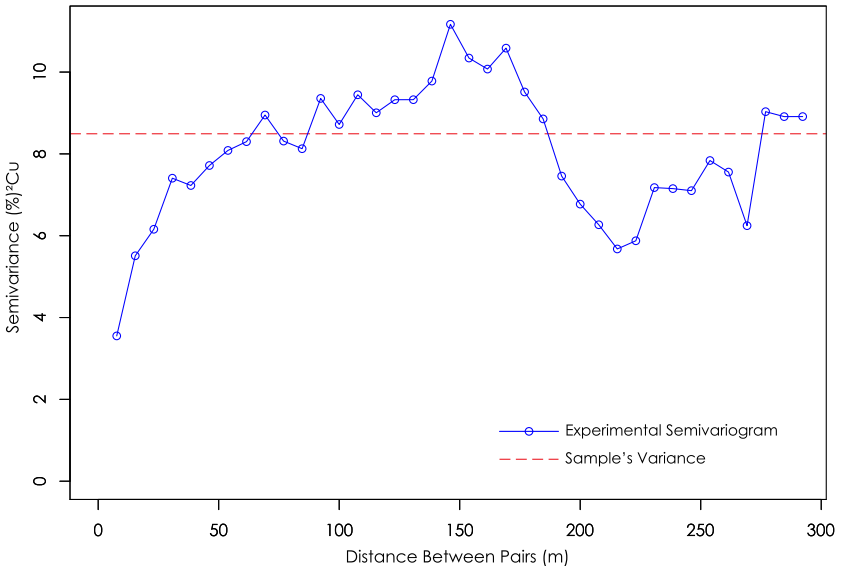

Figure 1. Example of an experimental semivariogram with the sample variance.

Mathematical functions for semivariogram fitting include, but are not limited to, spherical, exponential, and Gaussian ones, which are characterized by the existence of a sill (semivariance value) limiting the increase of the function.

Semivariogram models have three parameters defining their format (Figure 2): Nugget Effect, Sill, and Range. The first one is a chaotic or unstructured variance, and represents a variability much lower than the data spacing. The second means the variance of the data in the vector h, generally equal to the variance of these ones; and the latter is the distance from which there is no spatial correlation between the values [40, 43, 45]. All of these are necessary for the estimation based on kriging methods.

The indicator kriging is a nonlinear geostatistic method, where the prior appeal is to be nonparametric, not requiring the knowledge about the distribution being estimating [39, 43]. The method requires variables transformed in 0s and 1s, according to specific criteria (4). From the original distribution, K threshold values z_k are selected, and for each of them indicator variables are created, coding the values $Z(x)$ according to (4).

$$I(x, z_k) = \begin{cases} 1, & \text{if } Z(x) \leq z_k \\ 0, & \text{otherwise.} \end{cases} \tag{4}$$

The estimation of the values related to each indicator variable at the unsampled locations (without input data) is performed by several estimators, including the ordinary kriging one, which was the interpolation method used herein. In this case, the estimated values $I(x_0)$ are calculated as a linear combination (5) of the n input data $I(x_i)$ in the search neighborhood (elliptical shape), whose respective weights λ_i represent the spatial correlation between the estimated point (or block) and the input values inside the search ellipse, and used for the estimation [46].

$$I(x_0) = \sum_{i=1}^{n} \lambda_i I(x_i). \tag{5}$$

The calculation of the weights λ_i are based on the ordinary kriging system (6) that relates the semivariogram values between input data ($\gamma(x_i - x_j)$) and between input data and estimation

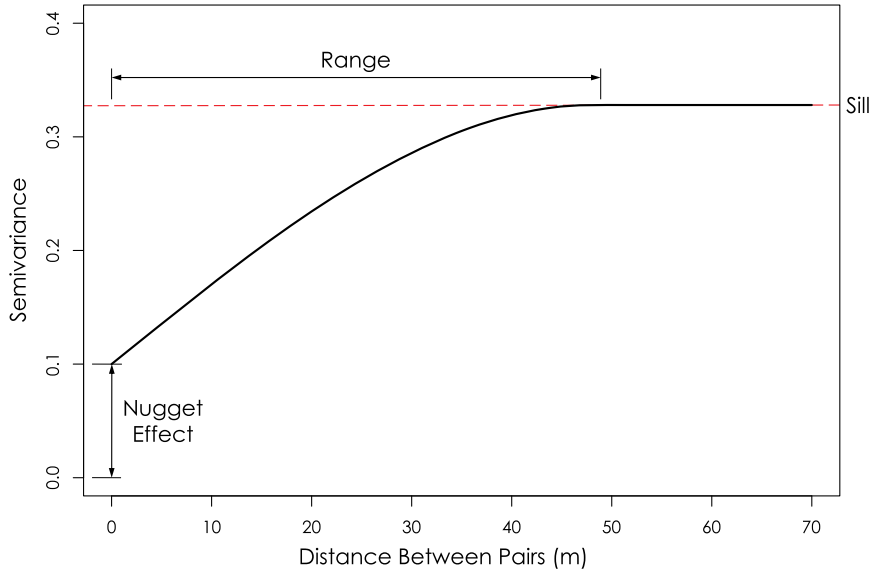

Figure 2. Spherical semivariogram model with its parameters. Horizontal red dashed line refers to the sample's variance.

point/block ($\gamma(x_i - x_0)$), and the Lagrange multiplier μ. The system can be expressed in a matrix form (7), from which the optimal weights are calculated [46].

$$\begin{cases} \displaystyle\sum_{j=1}^{n} \lambda_j \gamma(x_i - x_j) - \mu = \gamma(x_i - x_0) \quad \text{for } i = 1, \ldots, n \\ \displaystyle\sum_{j=1}^{n} \lambda_j = 1 \end{cases} \tag{6}$$

$$\begin{bmatrix} \lambda_1 \\ \lambda_2 \\ \vdots \\ \lambda_n \\ -\mu \end{bmatrix} = \begin{bmatrix} \gamma(x_1 - x_1) & \gamma(x_1 - x_2) & \cdots & \gamma(x_1 - x_n) & 1 \\ \gamma(x_2 - x_1) & \gamma(x_2 - x_2) & \cdots & \gamma(x_2 - x_n) & 1 \\ \vdots & \vdots & \ldots & \vdots & \vdots \\ \gamma(x_n - x_1) & \gamma(x_n - x_2) & \cdots & \gamma(x_n - x_n) & 1 \\ 1 & 1 & \cdots & 1 & 0 \end{bmatrix}^{-1} \begin{bmatrix} \gamma(x_0 - x_1) \\ \gamma(x_0 - x_2) \\ \vdots \\ \gamma(x_0 - x_n) \\ 1 \end{bmatrix}. \tag{7}$$

The ordinary kriging results in an estimation characterized to be theoretically unbiased, in the sense that the average estimation error is zero, and optimal, since the error variance is minimized [47] in such a way that the estimated values are optimal.

3. Materials and methods

For the study, in the 9.09 cm × 9.09 cm regular mesh (first scenario considered), 100 numerical damage metric data simulating real ones and based on the RMSD index were used, covering an aluminum plate of 100 cm × 100 cm (Figure 3). The damage metric values were defined in such a way that they represent real values when the plate has a failure in the center of it. It can be seen by the spatial variation of the numerical data in Figure 3, in which the highest values are located at the plates' center, while the lowest ones at the plate's borders.

The damage metric data was submitted to a statistical analysis, with the aim of identifying the principal characteristics of the distribution. In the sequence, four thresholds (z_i) of damage metric data (1, 2, 3, and 4) were defined to be used in the indicator kriging approach.

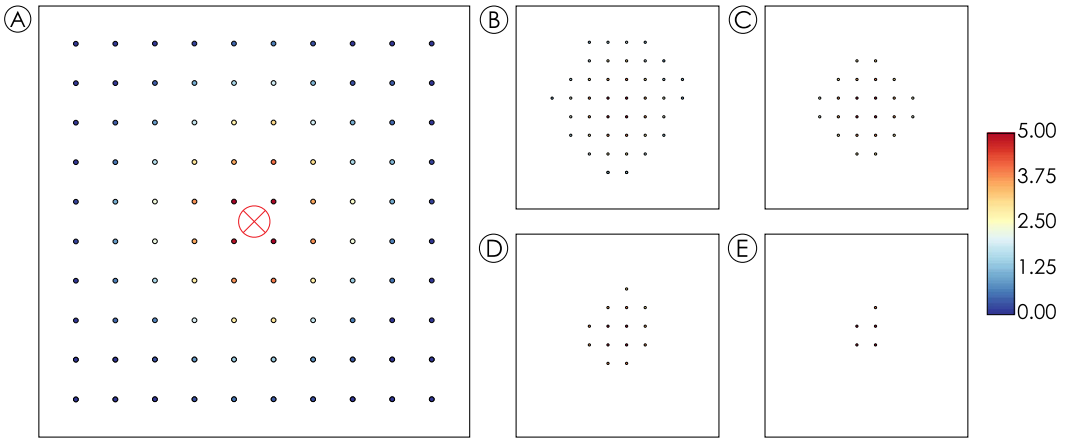

Figure 3. Localization of the numerical points at the plate (A), and damage metric values higher than 1 (B), 2 (C), 3 (D), and 4 (E). Red circle represents the damage's location.

The threshold equal to 4 is of particular interest, since the values higher than this one, are located near the damage. Based on these, four indicator variables (I_i) (binary values) were generated: one for each threshold, whose value attribution was based on (4).

Indicator variograms were calculated in several directions for each indicator variable, with the purpose of identifying the principal directions of continuity, which were the 0° and 90° azimuths. The experimental variograms of these directions were modeled, and the results, used to perform the indicator kriging.

The grid used to generate the estimates has unit cells of 4.0 cm × 4.0 cm dimensions, in such a way that the resolution of the model was 4.0 cm. The cell's dimension was defined in this way due to the following: (1) being smaller than all of the variographic ranges, and; (2) being a multiple of the plate size, which contributes to align the model with the dimensions of the plate.

Based on the numerical (input) data and the variographic information, the indicator kriging of the four thresholds (1, 2, 3, and 4) was performed, whose estimates of the indicator variables were based on the ordinary kriging method, with the aim of mapping local variations more appropriately. The search neighborhood used was circular, with a radius of 17.0 cm, whose value was equal to or lower than the variographic ranges in all indicator variables in such a way that the selected search neighborhood is an intersection of all possible search areas.

The results were given in the form of "probability below thresholds", due to the process of generation of the indicator variables (4). They were subtracted from 1 (maximum probability) for the calculation of the "probabilities above thresholds", which were used for the mapping of probability above these ones (1, 2, 3, and 4). The probability of the damage metric to be between threshold i and $i-1$ were defined as the difference between $P(i)$ and $P(i-1)$.

For the purpose of comparison between different spacing scenarios among PZT patches, four additional regular meshes were considered, based on numerical data (Figure 4): (1) 11.11 cm × 11.11 cm; (2) 14.286 cm × 14.286 cm; (3) 16.67 cm × 16.67 cm; and (4) 20.0 cm × 20.0 cm. In all cases, the damage was located in the center of the aluminum plate. The same procedures described previously were performed for each of the considered scenarios.

4. Results and discussions

The statistical analysis of the numerical data showed a highly asymmetric, positive skewed distribution (Figure 5), whose format was not determined (P-values lower than 0.01), possibly

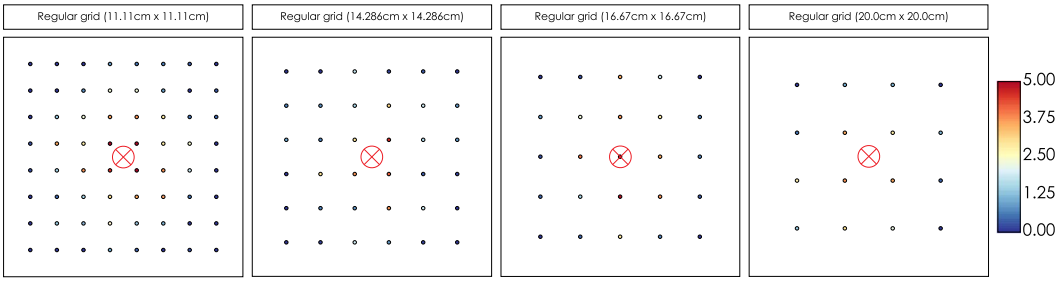

Figure 4. Different regular meshes illustrating the values of the damage metric data and the damage (red circle) in the center of the aluminum plate.

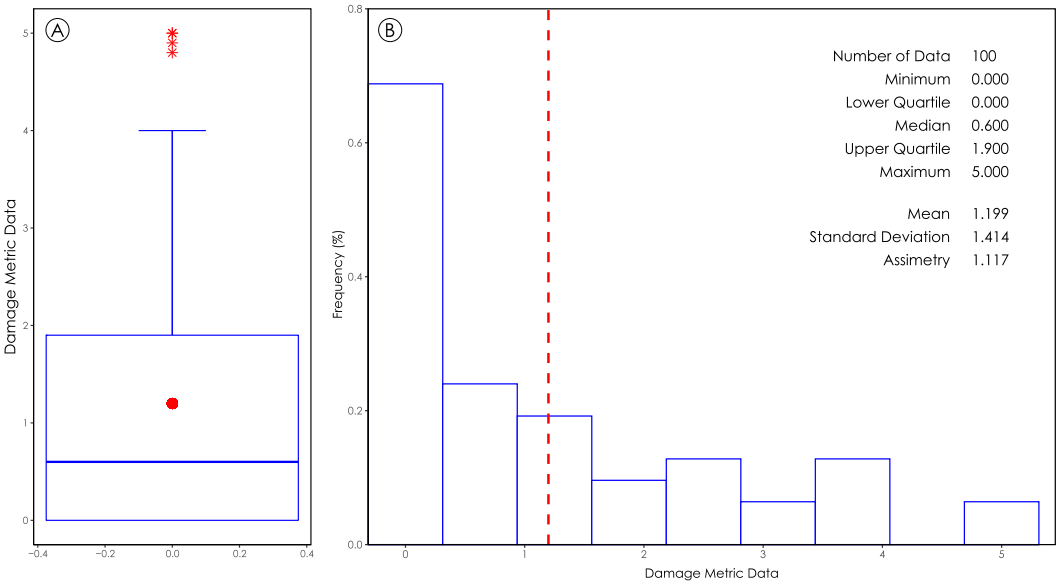

Figure 5. Box-plot (A) and histogram (B) of the damage metric data showing the mean value (red circular point and red dashed line) and outliers (red asterisk).

due to the limited amount of data. The presence of low damage metric values can also be seen by the quartiles, which shows that 50% of the data are lower than 0.6; 25% are between 0.6 and 1.9; and only 25% are higher than 1.9.

The extreme values (outliers) identified in the box-plot, all higher than 4, are directly associated to the damage's location, as they are located at the plate's center. Therefore, these are of fundamental importance for the prediction of the damage's position, which justifies the use of the threshold equal to 4 for this purpose.

The experimental semivariograms showed that the preferential directions of continuity were the North–South (Azimuth 0°) and East–West (Azimuth 90°), where the first was the direction of highest continuity for the thresholds 1 and 3 (geometric anisotropy), while in the other thresholds, there was not observed any anisotropy (Table 1). The existence of anisotropy in the semivariogram modeling can be an evidence of directional propagation of the failure and/or affected area, being useful for the mapping of this information.

The quality of the experimental semivariograms, given by the number and arrangement of the points in the graph, was higher in the case of the threshold equal to 1 (Figure 6), deteriorating

Table 1. Parameters of the semivariogram fitting for each indicator variable

Threshold	Indicator variable	Orientation	Nugget effect	Structure		
				Model	Contribution	Range (cm)
1	IND0	Azimuth 0°	0.01	Spherical	0.228	48.0
		Azimuth 90°	0.01	Spherical	0.228	30.0
2	IND1	Azimuth 0°	0.01	Gaussian	0.174	24.5
		Azimuth 90°	0.01	Gaussian	0.174	24.5
3	IND2	Azimuth 0°	0.00	Gaussian	0.114	22.0
		Azimuth 90°	0.00	Gaussian	0.114	19.0
4	IND3	Azimuth 0°	0.00	Gaussian	0.039	17.0
		Azimuth 90°	0.00	Gaussian	0.039	17.0

sequentially from the second to the fourth threshold. This is expected, since according to Rossi and Deutsch [43], thresholds much higher than the majority of the data can cause instabilities in experimental semivariograms.

It can also be observed that the models used in the semivariogram modeling were spherical (threshold equal to 1) and Gaussian (thresholds equal to 2, 3, and 4). This model reflects a phenomenon characterized by a much higher continuity in relation to the spherical one. In this way, despite the fact that the semivariogram ranges decreases as the thresholds become higher, located in the distribution's upper tail (thresholds equal to 3 and 4), the Gaussian model and the null nugget effect indicate a more continuous phenomenon in relation to the other situations. Due to the fact that 62% of the damage metric data are lower than 1, the resulting indicator kriging for this threshold value is characterized by having a much higher spatial variability in relation to the other ones, which is reflected by the shape of the semivariogram (spherical model) and its nugget effect, which represents 4.20% of the sill.

The semivariogram fitting of the indicator variable attributed to the threshold equal to 4 shows a modeling based on only one point of the experimental semivariogram. This is an expecting result, as indicator variables based on values much higher than the majority of data—in the upper tail of the distribution—may result in deteriorated semivariograms. However, an improvement in the semivariograms can be achieved when additional data are included in the analysis.

The performing of the indicator kriging resulted in maps of the probabilities of the damage metric to be: (1) higher than 1, 2, 3, and 4 (Figures 7a, c, e and g); (2) between 1 and 2 (Figure 7b); (3) between 2 and 3 (Figure 7d); and (4) between 3 and 4 (Figure 7f). Once the damage is located in the center of the plate, as the threshold value increases, the highest probabilities of the values to be higher than a particular threshold are sequentially restricted to the plate's center, converging the existence of these values limited to this site. Particularly in the case of the threshold equal to 4 (Figure 7g), the highest probabilities are restricted to the plate's center, where the damage is located, in such a way that the mapping of extreme values could predict the damages' locations.

On the other hand, the map related to the probability of the damage metric being higher than 1 (the lowest threshold value considered) shows an extensive area of high probability, being able to indicate the affected area due to the structural failure.

Therefore, information extracted by the probability maps can be used for mapping the area related to the existence of a structural failure (case of the threshold equal to 4) and/or affected by the failure (eventually the case of the threshold equal to 1), providing data for supporting the maintenance of the structure.

Comparing the mean values of the indicator variables in the model results with those in the numerical (sample) data (Figure 8), it can be seen that the respective mean values were

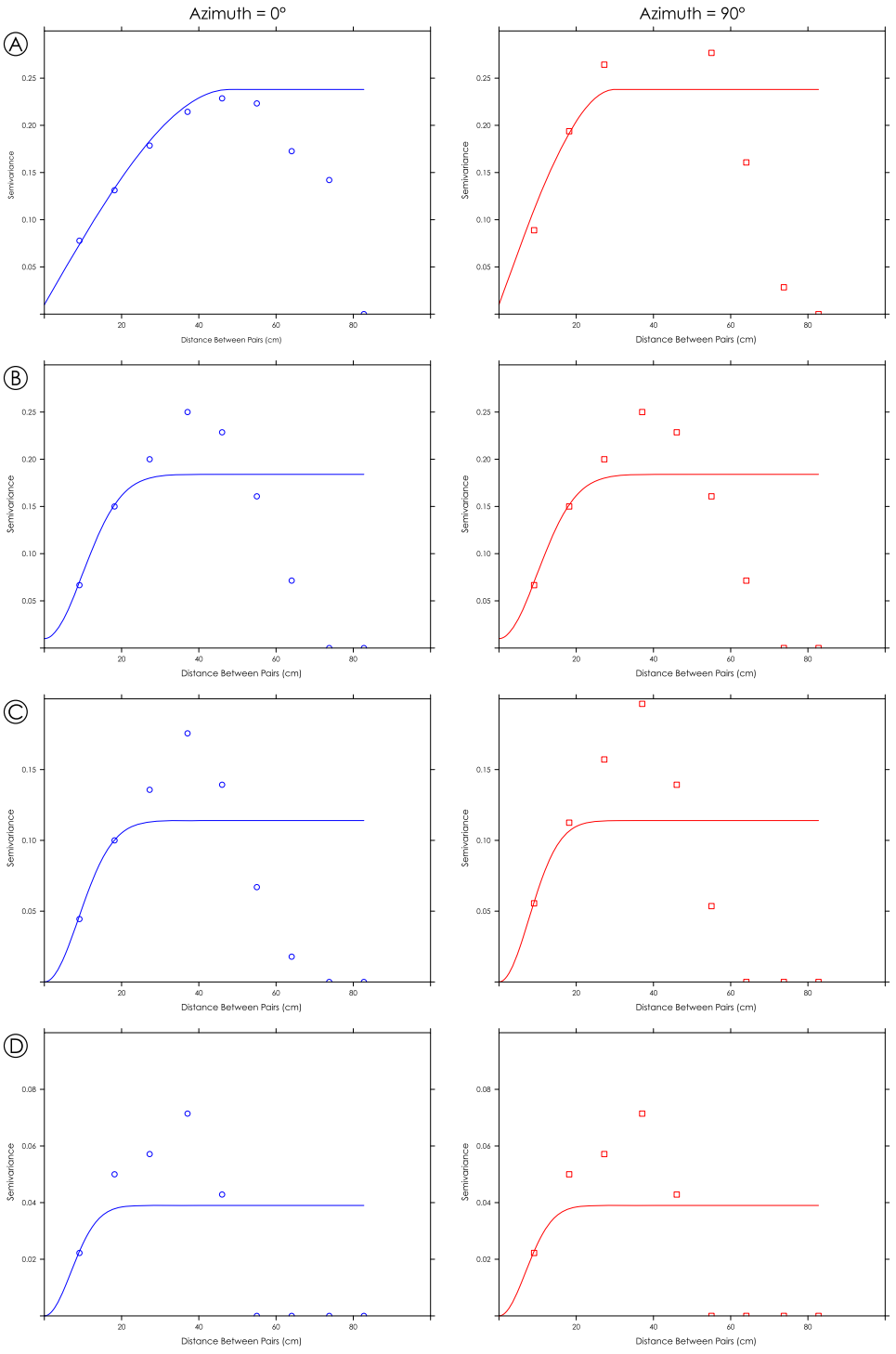

Figure 6. Experimental semivariogram and respective model fitting for each indicator variable and preferential direction of continuity. (A) IND0, (B) IND1, (C) IND2, and (D) IND3.

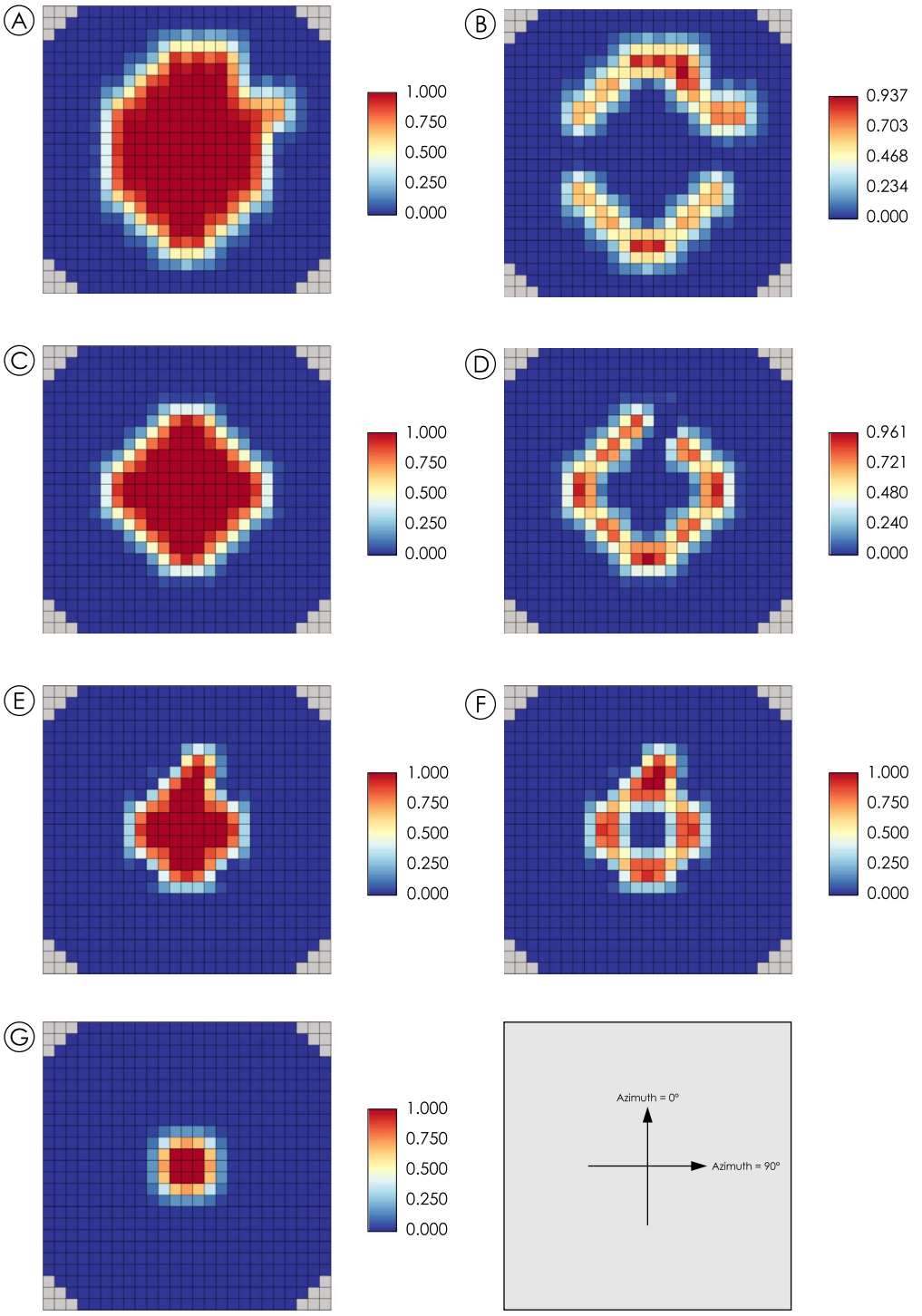

Figure 7. Probability maps of the damage metric values to be higher than 1 (A), 2 (C), 3 (E), 4 (G); and to be between 1 and 2 (B), between 2 and 3 (D), and between 3 and 4 (F).

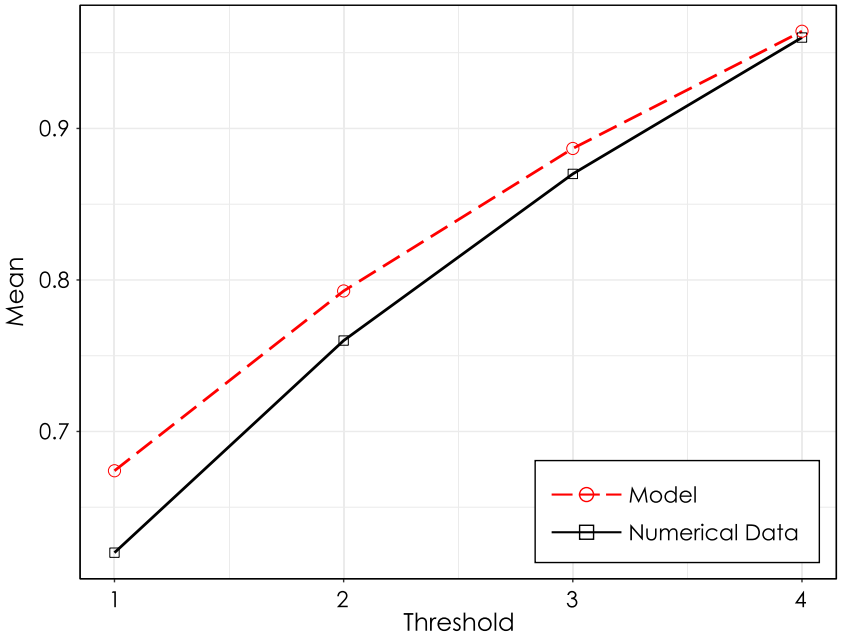

Figure 8. Mean values of the indicator variables related to their respective thresholds in the model and numerical (input) data.

approximately reproduced in the model, since the highest difference was 8.72%, attributed to the threshold equal to 1. This deviation could be a consequence of the higher spatial variability of this situation in relation to the other thresholds. The lower deviation (0.43%) was attributed to the threshold equal to 4, despite the low reliability of its experimental semivariogram, which can be a consequence of the high continuity of this scenario, with probabilities higher than 0 strictly limited to the plate's center, where the damage is located.

The mapping of the probability below thresholds between model and numerical data by bands in X (East–West) and Y (North–South) directions of the plate (Figure 9) shows that the model approximately reproduces the input data. The reproducibility is apparently lower for low threshold values, and sequentially higher for the high ones. It is possible to note that the spatial distribution of the values in the model is smoothed in relation to the numerical data, which is a consequence of the smooth effect of the estimator, presented as an inherent characteristic of the kriging methods.

Figure 10 illustrates the probability maps above thresholds for scenarios with regular spacing of 9.09 cm and 11.11 cm. In this figure, it is possible to verify the reduction of the model's reliability in the 11.11 cm scenario, observed by the occurrence of probability values more distant from the extremes (0 and 1). This behavior is more accentuated at the thresholds equal to 1, 2, and 3. For the threshold equal to 4, specifically in the damage region, there was no significant loss reliability, being able to accurately predict the location of the failure. Thus, it can be concluded that the ability to predict the occurrence of damage was not impaired by increasing the spacing from 9.09 cm to 11.11 cm.

The greatest loss of reliability for the thresholds equal to 1, 2, and 3 in the 11.11 cm scenario may be due to the greater spatial variability between the values of the respective indicator variables, as the sample variances were 0.248, 0.218, and 0.145, respectively. This does not occur with the threshold equal to 4 because there are few damage metric values greater than 4, resulting in a sample variance equal to 0.060.

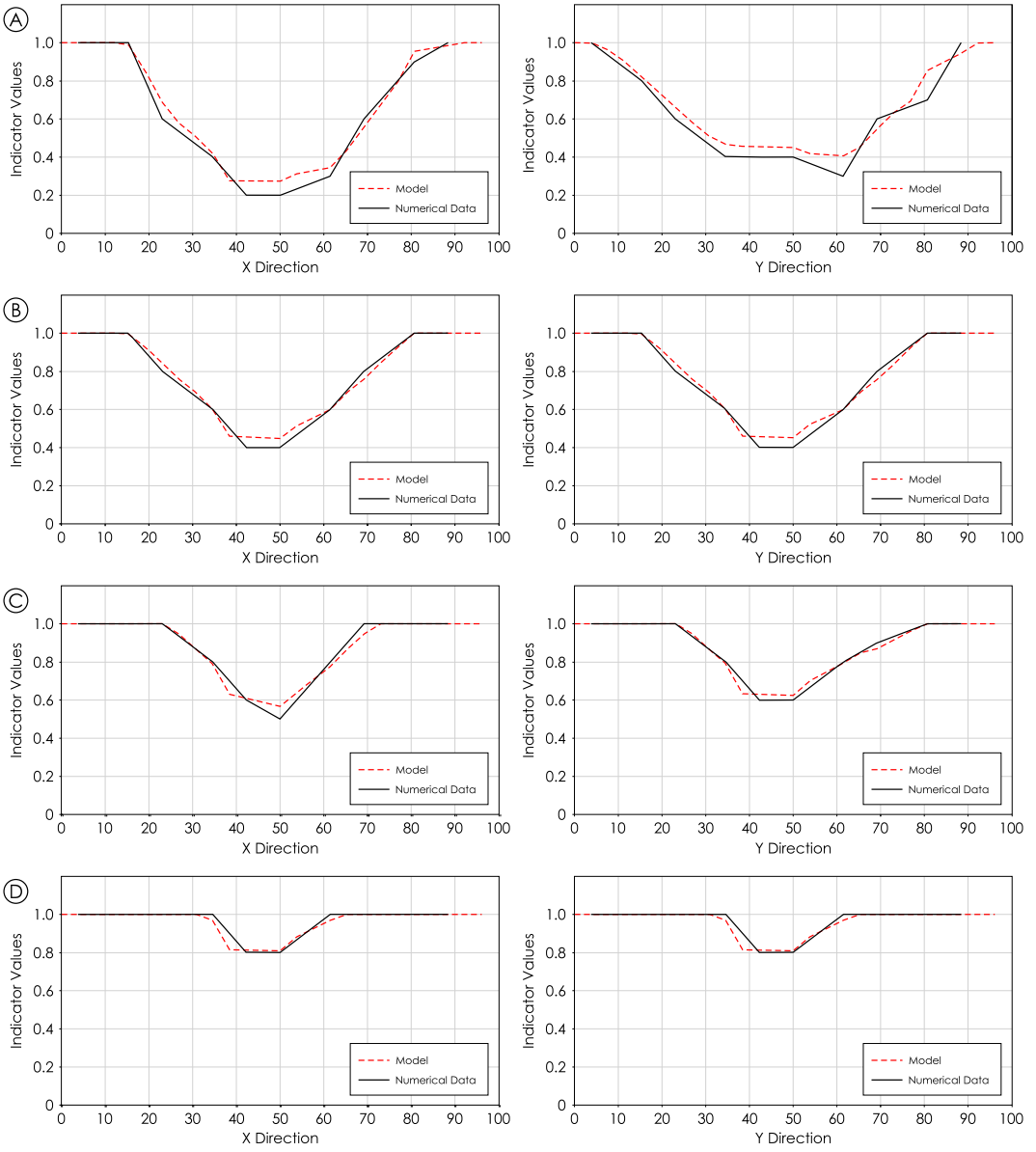

Figure 9. Swath plots of the indicator variables comparing the model results with the input data in X and Y directions: (A) threshold equal to 1 (IND0); (B) threshold equal to 2 (IND1); (C) threshold equal to 3 (IND2); and (D) threshold equal to 4 (IND3).

Figure 11 presents the maps of probability above thresholds for the scenarios with regular spacing of 14.286 cm and 16.67 cm. In these cases, it is possible to verify the increase in the reliability of the results from the 14.286 cm to 16.67 cm scenarios, evidenced by the occurrence of probability values closer to the extremes (0 and 1) with the increase of the damage metric data spacing. This can be explained as a consequence of the presence of a damage metric value overlapping the fault location (center of the plate) for the 16.67 cm spacing scenario, which does not occur for the 14.286 cm mesh.

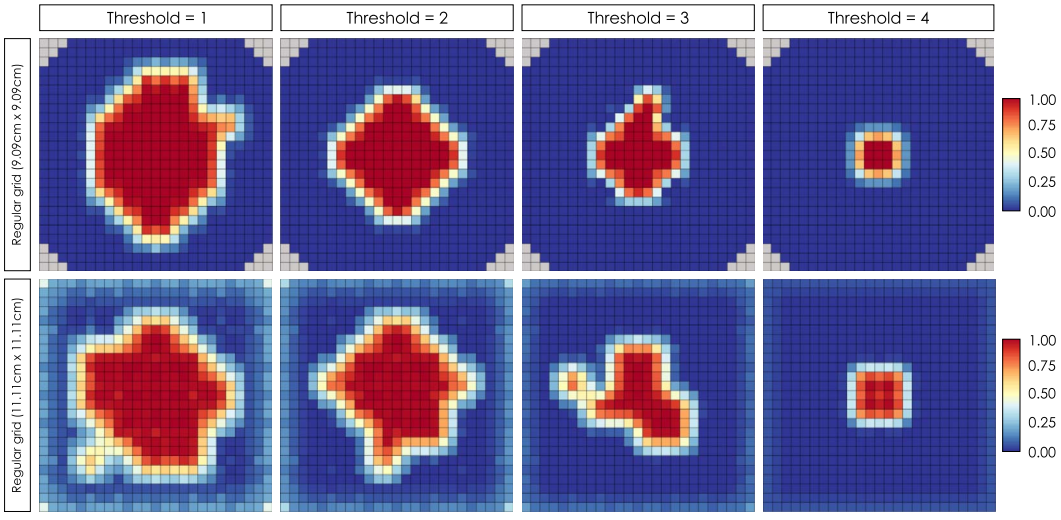

Figure 10. Probability maps for values above thresholds for scenarios with regular meshes of 9.09 cm and 11.11 cm.

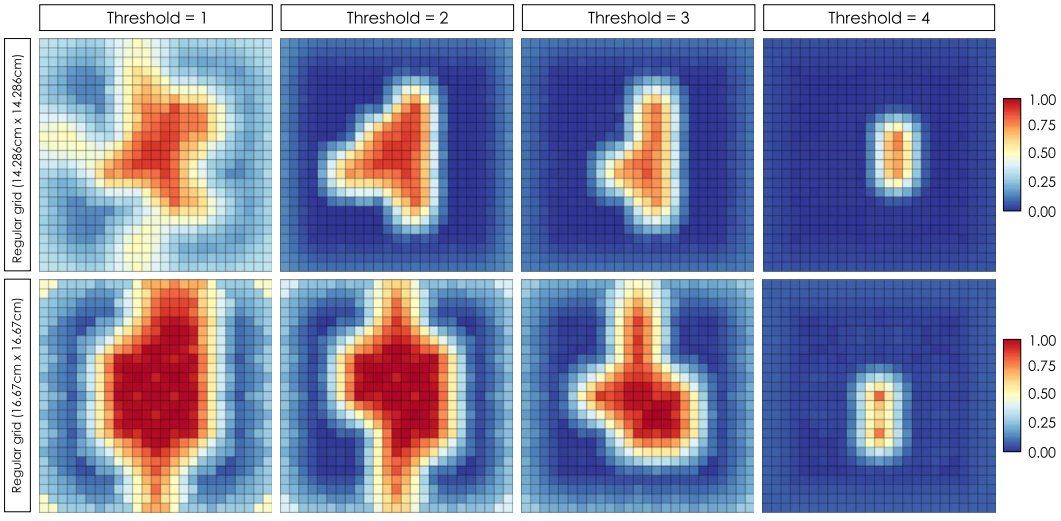

Figure 11. Probability maps for values above thresholds for scenarios with regular meshes of 14.286 cm and 16.67 cm.

The results for the threshold equal to 4 show less ability to predict the position of the damage in the center of the plate for these models when compared with the aforementioned results. This occurs due to the greater distance between the sampled points in these scenarios. The 16.67 cm spacing scenario showed a more adequate result in relation to the 14.286 cm one, probably due to sampling overlapping the failure site. However, in general conditions of failure in several positions, the result of this condition could be less reliable in relation to the other considered scenarios.

For the scenario with a regular spacing of 20 cm, it was not possible to obtain experimental semivariograms, and, therefore, perform the indicator kriging. This represents that for the structure under study, due to its size and geometry, it is not possible to obtain models to predict

failure occurrence sites for meshes with spacing greater than 16.67 cm. This was a procedure evaluated in this contribution to define some criteria for limiting the sampling distribution of the impedance signatures of the PZT patches. However, this same trial procedure must be conducted for each specific structure to be studied.

5. Conclusions

Concluding, it was possible to map the probabilities of occurrence of several damage metric intervals in a mesh of sensors enabling the possibility of damage detection by the use of indicator kriging. Especially, the probability model based on the threshold equal to 4 showed that the highest probabilities—to be higher than 4—were strictly limited to the plate's center, where the damage is located. Therefore, from this approach, it is possible to delineate the damage's position from mapping the probabilities of damage metric values to be higher than the extreme ones (outliers).

The geometric anisotropy observed in the semivariograms probably is an indicative of preferential directions of the damage's propagation, and can be useful to acquire this information. However, this question needs additional research, with the aim of validating this one.

The model approximately reproduced the input numerical data, given the low differences observed between the model and sample means of the indicator variables. Furthermore, the swath plots in the X and Y directions show the capacity of the model to predict the input values, despite the smooth effect inherent of the estimation methods based on kriging.

The analysis of scenarios based on different spacing of PZT patches showed that the increase in the damage metric data spacing caused a loss of reliability of the model to predict the location of the structural failure. This was more pronounced in the meshes with spacing of 14.286 cm and 16.67 cm. However, even in these scenarios, it would be possible to identify the approximate position of the damage.

The impossibility of obtaining experimental variograms for the scenario with a 20 cm spacing between PZT patches showed a limiting factor in the methodology. However, although it is a trial procedure, it can be applied to other dimensions and geometries of structures to identify the minimum number of sensors/actuators as well as their arrangement on the plate.

The information obtained in the probabilities' mapping can be useful to identify the location of failure sources and/or affected areas due to a structural failure. However, future contributions should focus on producing different damage locations as well as different severities in order to have more quantitative results to improve the decision-making process. This incipient contribution aims to present the initial possibilities, case study, and applicability to join geostatistic tools to the SHM.

References

[1] C. Boller, "Structural health monitoring—an introduction and definitions", in *Encyclopedia of Structural Health Monitoring* (C. Boller, F.-K. Chang, Y. Fujino, eds.), John Wiley & Sons, Ltd., Houston, 2009, p. 1-23.

[2] R. A. Antunes, N. E. Cortez, B. M. Gianesini, J. Vieira Filho, "Modeling, simulation, experimentation, and compensation of temperature effect in impedance-based SHM systems applied to steel pipes", *Sensors* **19** (2019), p. 1-23.

[3] A. Martowicz, A. Sendecki, M. Salamon, M. Rosiek, T. Uhl, "Application of electromechanical impedance-based SHM for damage detection in bolted pipeline connection", *Nondestruct. Test. Eval.* **31** (2016), p. 17-44.

[4] I. I. C. Maruo, G. de Faria Giachero, V. Steffen Jr., R. M. Finzi Neto, "Electromechanical impedance—based structural health monitoring instrumentation system applied to aircraft structures and employing a multiplexed sensor array", *J. Aerosp. Technol. Manage.* **7** (2015), no. 3, p. 294-306.

[5] P. Selva, O. Cherrier, V. Budinger, F. Lachaud, J. Morlier, "Smart monitoring of aeronautical composites plates based on electromechanical impedance measurements and artificial neural networks", *Eng. Struct.* **56** (2013), p. 794-804.

[6] H. Boukabache, C. Escriba, S. Zedek, D. Medale, S. Rolet, J. Y. Fourniols, "System-on-chip integration of a new electromechanical impedance calculation method for aircraft structure health monitoring", *Sensors* **12** (2012), no. 10, p. 13617-13635.
[7] L. V. Palomino, J. R. V. Moura Jr., K. M. Tsuruta, D. A. Rade, V. Steffen Jr., "Impedance-based health monitoring and mechanical testing of structures", *Smart Struct. Syst.* **7** (2011), no. 1, p. 15-25.
[8] J. R. V. Moura Jr., V. Steffen Jr., "Impedance-based health monitoring for aeronautic structures using statistical metamodeling", *J. Intell. Mater. Syst. Struct.* **17** (2006), no. 11, p. 1023-1036.
[9] C. Zhang, Q. Yan, G. P. Panda, W. Wu, G. Song, C. Vipulanandan, "Real-time monitoring stiffness degradation of hardened cement paste under uniaxial compression loading through piezoceramic-based electromechanical impedance method", *Constr. Build. Mater.* **256**, no. 2020, p. 119395-119410.
[10] Y.-F. Su, G. Han, A. Amran, T. Nantung, N. Lu, "Instantaneous monitoring the early age properties of cementitious materials using PZT-based electromechanical impedance (EMI) technique", *Constr. Build. Mater.* **136**, no. 2019, p. 340-347.
[11] W. W. Peng Liu, Y. Chen, X. Feng, L. Miao, "Concrete damage diagnosis using electromechanical impedance technique", *Constr. Build. Mater.* **136** (2017), p. 450-455.
[12] H. Kim, X. Liu, E. Ahn, M. Shin, S. W. Shin, S.-H. Sim, "Performance assessment method for crack repair in concrete using PZT-based electromechanical impedance technique", *NDT&E Int.* **104** (2019), p. 90-97.
[13] Y. Yang, B. S. Divsholi, "Sub-frequency interval approach in electromechanical impedance technique for concrete structure health monitoring", *Sensors* **10** (2010), no. 12, p. 11644-11661.
[14] Y. Yang, B. S. Divsholi, C. K. Soh, "A reusable PZT transducer for monitoring initial hydration and structural health of concrete", *Sensors* **10** (2010), no. 5, p. 5193-5208.
[15] H. Kima, X. Liub, E. Ahna, M. Shina, S. W. Shinc, S.-H. Sima, "Performance assessment method for crack repair in concrete using PZT-based electromechanical impedance technique", *NDT&E Int.* **104** (2019), p. 90-97.
[16] S. Na, H. K. Lee, "Neural network approach for damaged area location prediction of a composite plate using electromechanical impedance technique", *Compos. Sci. Technol.* **88** (2013), p. 62-68.
[17] J. Zhu, Y. Wang, X. Qing, "Modified electromechanical impedance-based disbond monitoring for honeycomb sandwich composite structure", *Compos. Struct.* **217** (2019), p. 175-185.
[18] D. Ai, H. Zhu, H. Luo, J. Yang, "An effective electromechanical impedance technique for steel structural health monitoring", *Constr. Build. Mater.* **73** (2014), p. 97-104.
[19] H. A. Tinoco, L. Robledo-Callejas, D. J. Marulanda, A. L. Serpa, "Damage detection in plates using the electromechanical impedance technique based on decoupled measurements of piezoelectric transducers", *J. Sound Vib.* **384** (2016), p. 146-162.
[20] S. Na, H. Lee, "Steel wire electromechanical impedance method using a piezoelectric material for composite structures with complex surfaces", *Compos. Struct.* **98** (2013), p. 79-84.
[21] J. Zhu, X. Qing, X. Liu, Y. Wang, "Electromechanical impedance-based damage localization with novel signatures extraction methodology and modified probability-weighted algorithm", *Mech. Syst. Signal Process.* **146** (2021), p. 210-220.
[22] C. Kralovec, M. Schagerl, M. Mayr, "Localization of damages by model-based evaluation of electro-mechanical impedance measurements", *Eur. Workshop Struct. Health Monit.* **9** (2018), p. 1-12.
[23] P. S. Olivier Cherrier, V. Pommier-Budinger, F. Lachaud, J. Morlier, "Damage localization map using electromechanical impedance spectrums and inverse distance weighting interpolation: Experimental validation on thin composite structures", *Struct. Health Monit.* **12** (2013), p. 311-324.
[24] D. R. Gonçalves, J. R. V. Moura Jr., P. E. C. Pereira, "Monitoramento de integridade estrutural baseado em impedância eletromecânica utilizando o método de krigagem ordinária", *HOLOS* **36** (2020), no. 2, p. 1-17.
[25] B. Lin, V. Giurgiutiu, "Modeling and testing of PZT and PVDF piezoelectric wafer active sensors", *Smart Mater. Struct.* **15** (2006), no. 4, p. 1085-1093.
[26] G. Park, H. Sohn, C. R. Farrar, D. J. Inman, "Overview of piezoelectric impedance-based health monitoring and path forward", *Shock Vib. Dig.* **35** (2003), no. 6, p. 451-463.
[27] C. Liang, F. P. Sun, C. A. Rogers, "Coupled electro-mechanical analysis of adaptive material systems—determination of the actuator power consumption and system energy transfer", *J. Intell. Mater. Syst. Struct.* **5** (1994), no. 1, p. 12-20.
[28] S. Bhalla, C. K. Soh, "Electro-Mechanical Impedance Technique", in *Smart Materials in Structural Health Monitoring, Control and Biomechanics* (C.-K. Soh, Y. Yang, S. Bhalla, eds.), Advanced Topics in Science and Technology in China, Springer+Business Media, 2012, p. 17-51.
[29] F. G. Baptista, J. Vieira Filho, "Optimal frequency range selection for PZT transducers in impedance-based SHM systems", *IEEE Sens. J.* **10** (2010), no. 8, p. 1297-1303.
[30] A. N. Zagrai, V. Giurgiutiu, "Electromechanical impedance modeling", in *Encyclopedia of Structural Health Monitoring* (C. Boller, F.-K. Chang, Y. Fujino, eds.), John Wiley & Sons Ltd., Houston, 2009, p. 71-89.
[31] D. M. Peairs, P. A. Tarazaga, D. J. Inman, "Frequency range selection for impedance-based structural health monitoring", *J. Vib. Acoust.* **129** (2007), no. 6, p. 701-709.

[32] D. M. Peairs, D. J. Inman, G. Park, "Circuit analysis of impedance-based health monitoring of beams using spectral elements", *Struct. Health Monit.* **6** (2007), no. 1, p. 81-94.
[33] V. Giurgiutiu, *Structural Health Monitoring with Piezoelectric Wafer Active Sensors*, vol. 2, Academic Press, Waltham, MA, 2014, 1024 pages.
[34] V. Giurgiutiu, C. A. Rogers, "Recent advancements in the electromechanical (E/M) impedance method for structural health monitoring and NDE", in *Smart Structures and Materials 1998: Smart Structures and Integrated Systems* (M. E. Regelbrugge, ed.), vol. 3329, International Society for Optics and Photonics, SPIE, Bellingham, WA, 1998, p. 536-547.
[35] G. Matheron, "Principles of geostatistics", *Econom. Geol.* **58** (1963), p. 1246-1266.
[36] G. Matheron, "Kriging, or polynomial interpolation procedures? A contribution to polemics in mathematical geology", *Can. Min. Metall. Trans.* **70** (1967), p. 240-244.
[37] G. Matheron, "The theory of regionalized variables and its applications", in *Les cahiers du Centre de Morphologie Mathématique de Fontainebleau*, vol. 05, École Nationale Supérieure des Mines de Paris, Paris, France, 1971.
[38] J.-P. Chilès, P. Delfiner, *Geostatistics: Modeling Spatial Uncertainty*, 2nd ed., John Wiley & Sons, Hoboken, USA, 2012.
[39] M. B. Revuelta, "Mineral resource evaluation", in *Mineral Resources: From Exploration to Sustainability Assessment*, Springer Textbooks in Earth Sciences, Geography and Environment, Springer International Publishing AG, Cham, Switzerland, 2018, p. 223-309.
[40] A. G. Journel, C. J. Huijbregts, *Mining Geostatistics*, Academic Press Limited, London, UK, 1978.
[41] A. J. Sinclair, G. H. Blackwell, "Spatial (structural) analysis: an introduction to semivariograms", in *Applied Mineral Inventory Estimation*, Cambridge University Press, Cambridge, UK, 2004, p. 192-214.
[42] M. Abzalov, "Variography", in *Applied Mining Geology, Modern Approaches in Solid Earth Sciences*, vol. 12, Springer International Publishing AG, Cham, Switzerland, 2016, p. 239-262.
[43] M. E. Rossi, C. V. Deutsch, *Mineral Resource Estimation*, Springer Science+Business Media, Dordrecht, Netherlands, 2014.
[44] P. K. Kitanidis, "Intrinsic model", in *Introduction to Geostatistics: Applications in Hydrogeology*, Cambridge University Press, Cambridge, UK, 1997, p. 41-82.
[45] W. A. Hustrulid, M. Kuchta, R. K. Martin, "Orebody description", in *Open Pit Mine Planning & Design*, vol. 1, CRC Press, London, UK, 3rd ed., 2013, p. 186-289.
[46] J. K. Yamamoto, P. M. B. Landim, "Estimativas Geoestatísticas", in *Geoestatística: Conceitos e Aplicações*, Oficina de Textos, São Paulo, Brazil, 1st ed., 2013, p. 55-119.
[47] E. H. Isaaks, R. M. Srivastava, "Ordinary kriging", in *Applied Geostatistics*, Oxford University Press, New York, USA, 1st ed., 1989, p. 278-322.